Supporting Information

Synthesis of Octahedral Pt-Ni-Ir Yolk-Shell Nanoparticles and their Catalysis for Oxygen Reduction and Methanol Oxidization in both Acidic and Alkaline Conditions

Tao Yang,[a,] Yihui Wang,[a] Wenxian Wei,[b] Xinran Ding,[a] Maoshuai He,[c,d] Tingting Yu,[a] Hong Zhao,[a] Dongen Zhang[a]*

[a]School of Chemical Engineering, Jiangsu Ocean University, Lianyungang 222005, China

[b]Testing Center, Yangzhou University, Yangzhou 225009, China

[c]State Key Laboratory of Eco-Chemical Engineering, Ministry of Education, College of Chemistry and Molecular Engi-neering, Qingdao University of Science and Technology, Qingdao 266042, China

[d]School of Materials Science and Engineering, Shandong University of Science and Technology, Qingdao 266590, China

Correspondence and requests for materials should be addressed to Tao Yang (yangtao_hit@163.com)

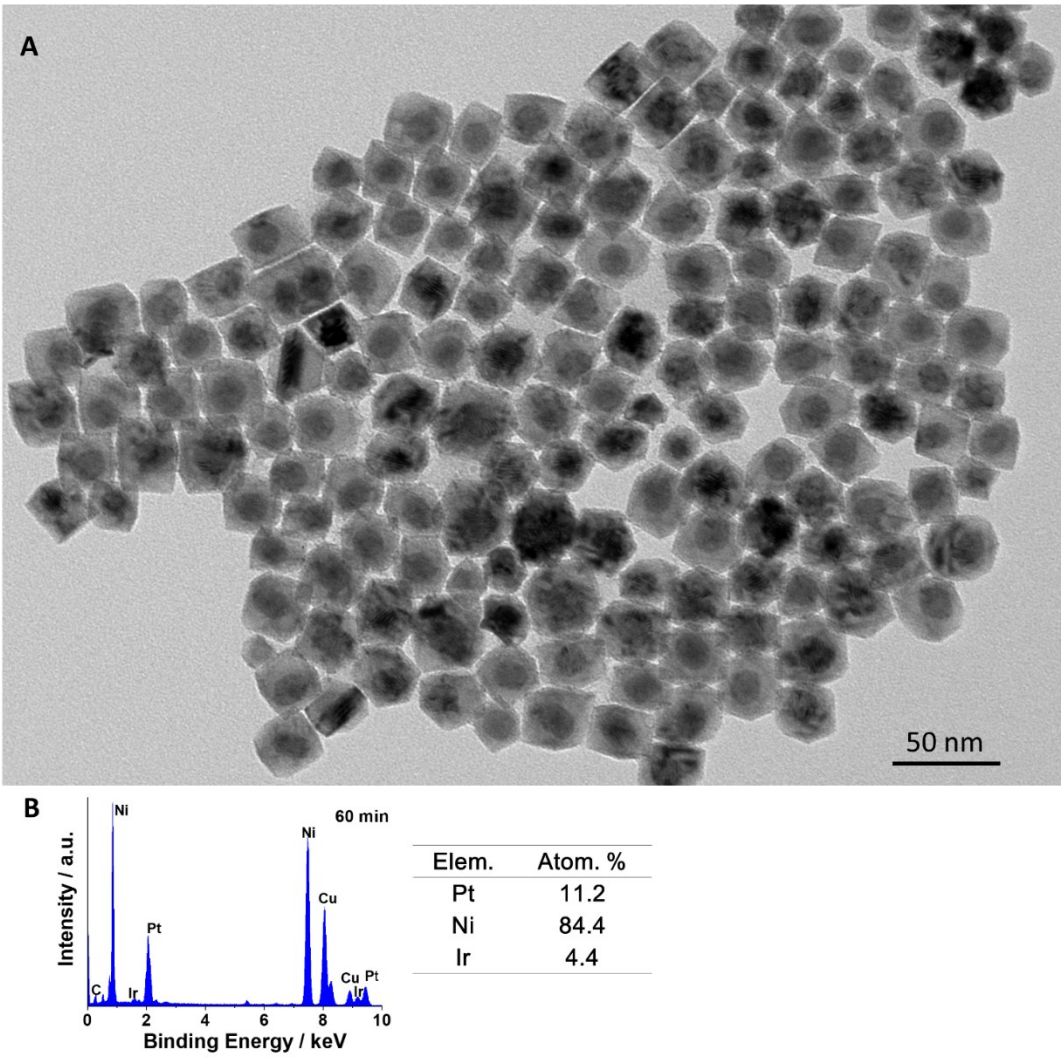

Elem.	Atom. %
Pt	11.2
Ni	84.4
Ir	4.4

Fig. S1 (A) TEM image of the Pt-Ni-Ir core-shell nanoparticles obtained by reducing $Pt(acac)_2$, $Ni(acac)_2$ and $Ir(acac)_3$ with carbon monoxide in oleylamine（OAm) and oleic acid (OA) at 230 ℃ for 60 min, and (B) the corresponding TEM-EDS spectra. Nearly all the products are core-shell nanoparticles (~25 nm in edge length) with a dark core and an octahedral shell. The chemical composition calculated from TEM-EDS spectra was also shown.

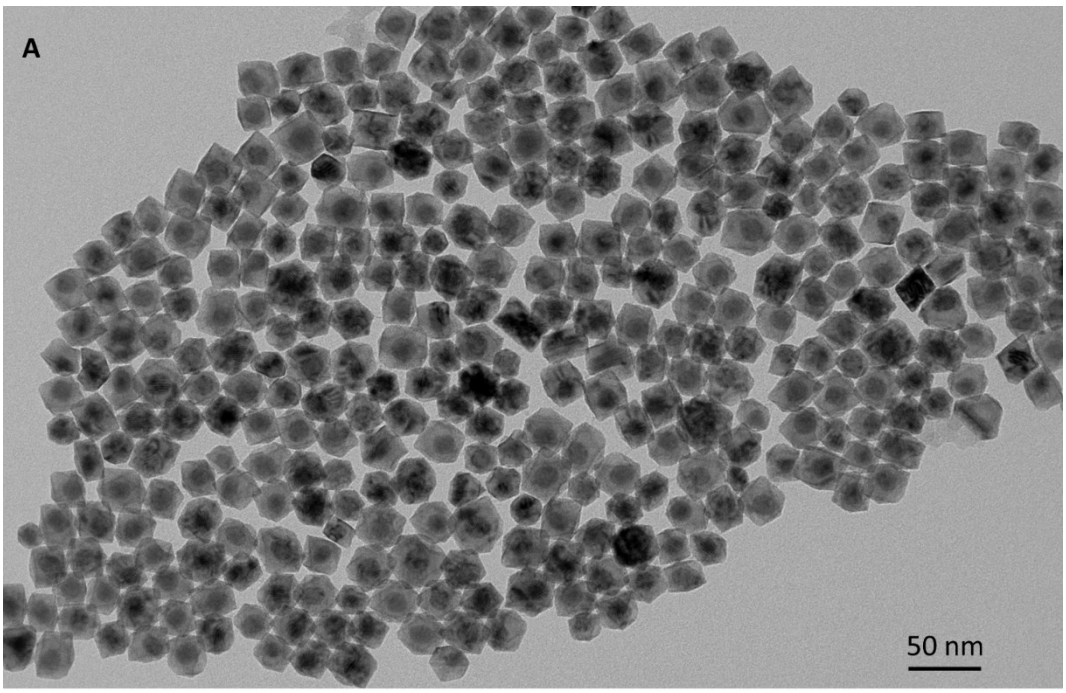

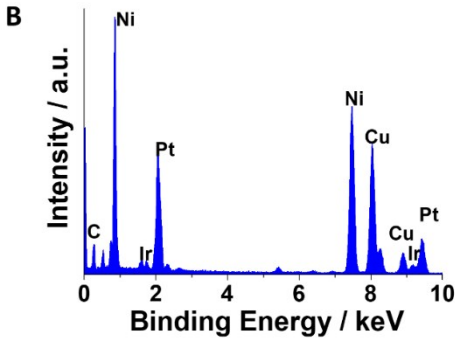

Elem.	Atom. %
Pt	19.5
Ni	76.3
Ir	4.2

Fig. S2 (A) TEM image of the Pt coved nanoparticles by controllably depositing Pt on Pt-Ni-Ir core-shell, and (B) the corresponding TEM-EDS spectra. The products are still core-shell nanoparticles with similar size. The chemical composition obtained from TEM-EDS spectra shows the increment of Pt content compared with the Pt-Ni-Ir core-shell. There are no isolated Pt nanoparticles. These results suggest that Pt exclusively deposited on the Pt-Ni-Ir core-shell nanoparticles in the second process.

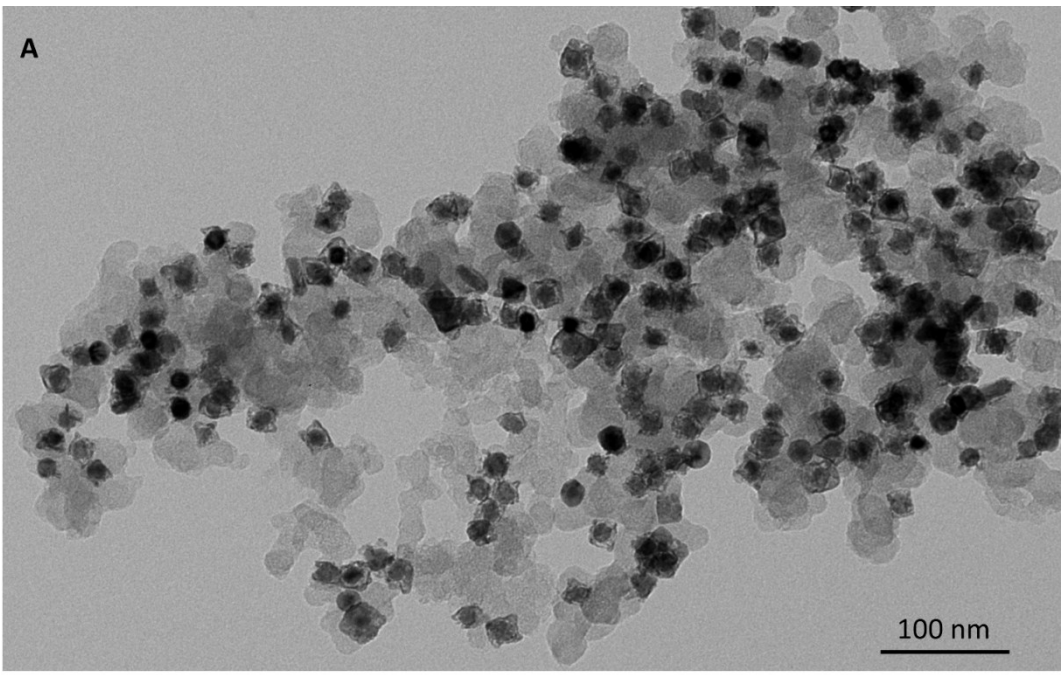

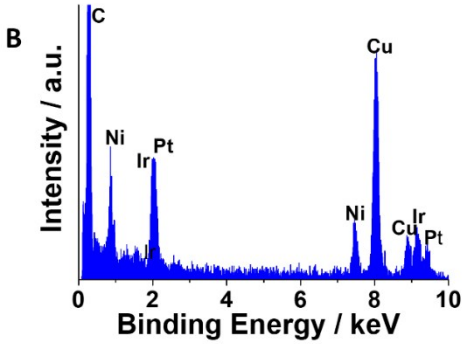

Elem.	Atom. %
Pt	59.6
Ni	18.4
Ir	22.0

Fig. S3 (A) TEM image of the products obtained by Ni-coordinating etching the Pt covered Pt-Ni-Ir core-shell nanoparticles, and (B) the corresponding TEM-EDS spectra. The Ni-rich phase was removed and yolk-shell structure formed.

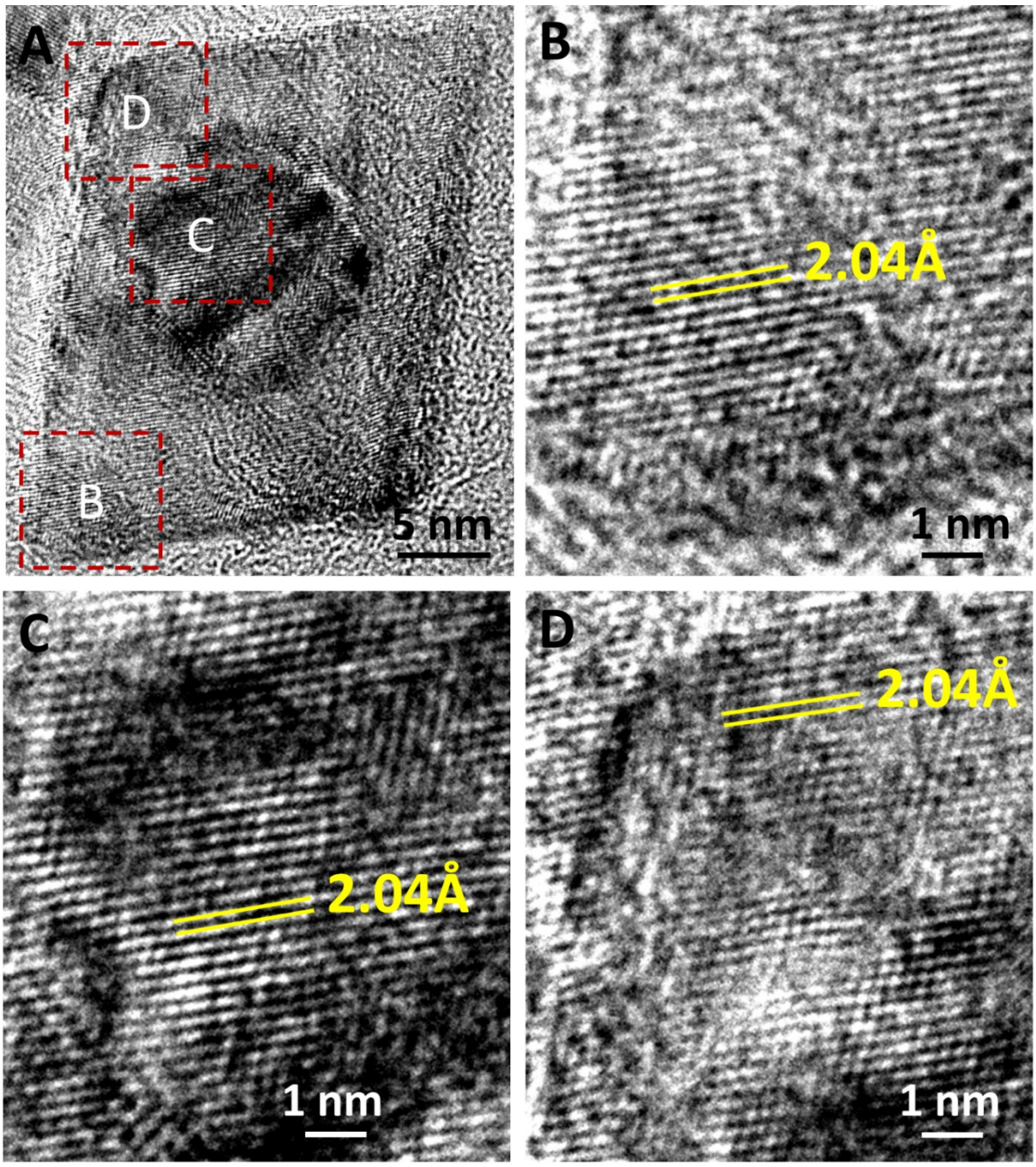

Fig. S4 (A) HRTEM image of an individual Pt-Ni-Ir core-shell octahedron, and (B-D) three enlarged region circled by red rectangles. The distinct lattice fringes with a *d*-spacing of 2.04 Å coherently extended over the whole crystal, suggesting that the nanoparticle was enclosed by Ni-rich nanocrystal with high crystallinity.

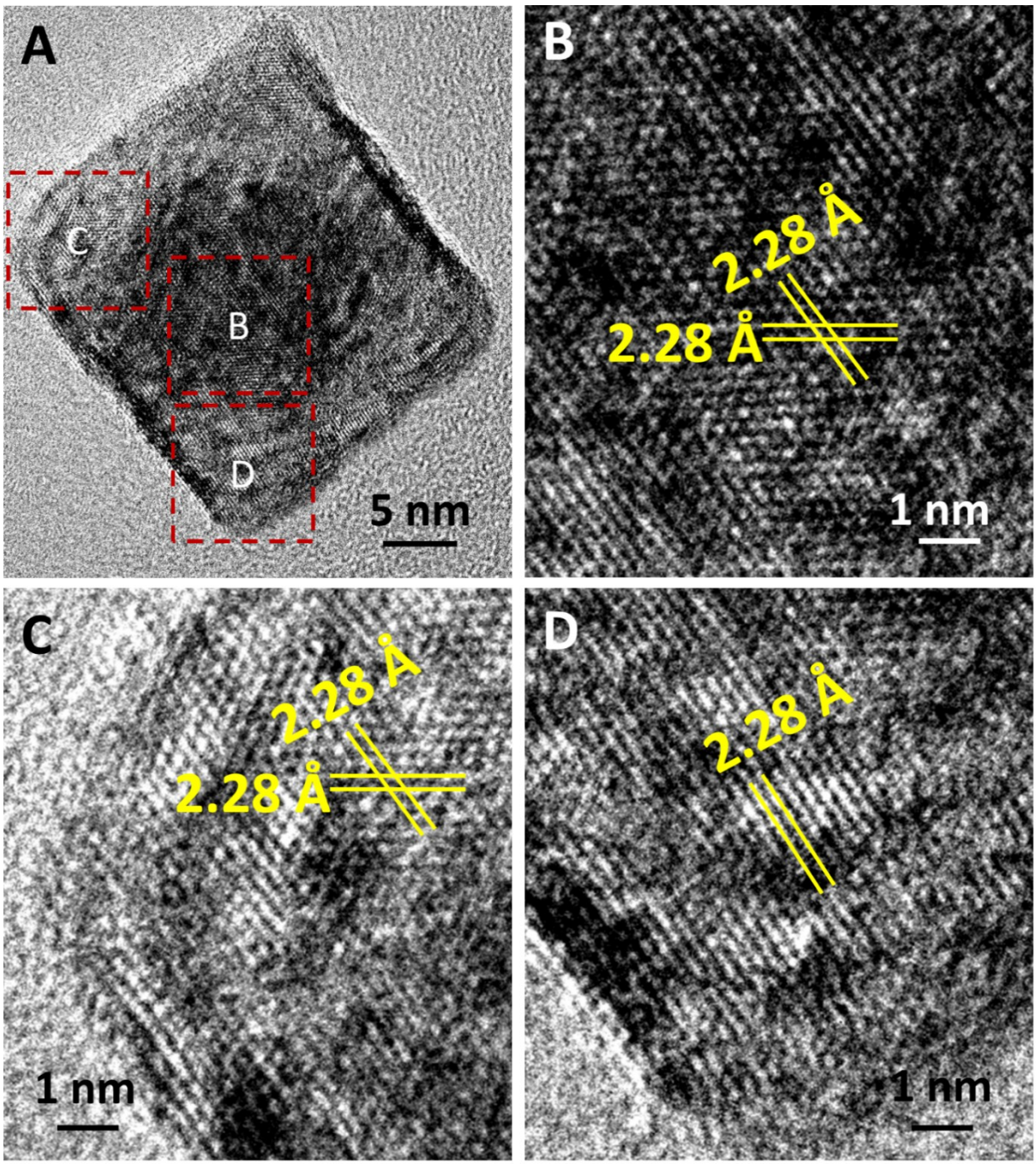

Fig. S5 (A) HRTEM image of an individual Pt covered Pt-Ni-Ir core-shell octahedron, and (B-D) three enlarged region circled by red rectangles. The distinct lattice fringes with a *d*-spacing of 2.28 Å coherently extended over the whole crystal, suggesting that the nanoparticle was enclosed by Pt-rich skin with high crystallinity. The scale bar in A is 5 nm, in B, C and D is 1 nm, respectively.

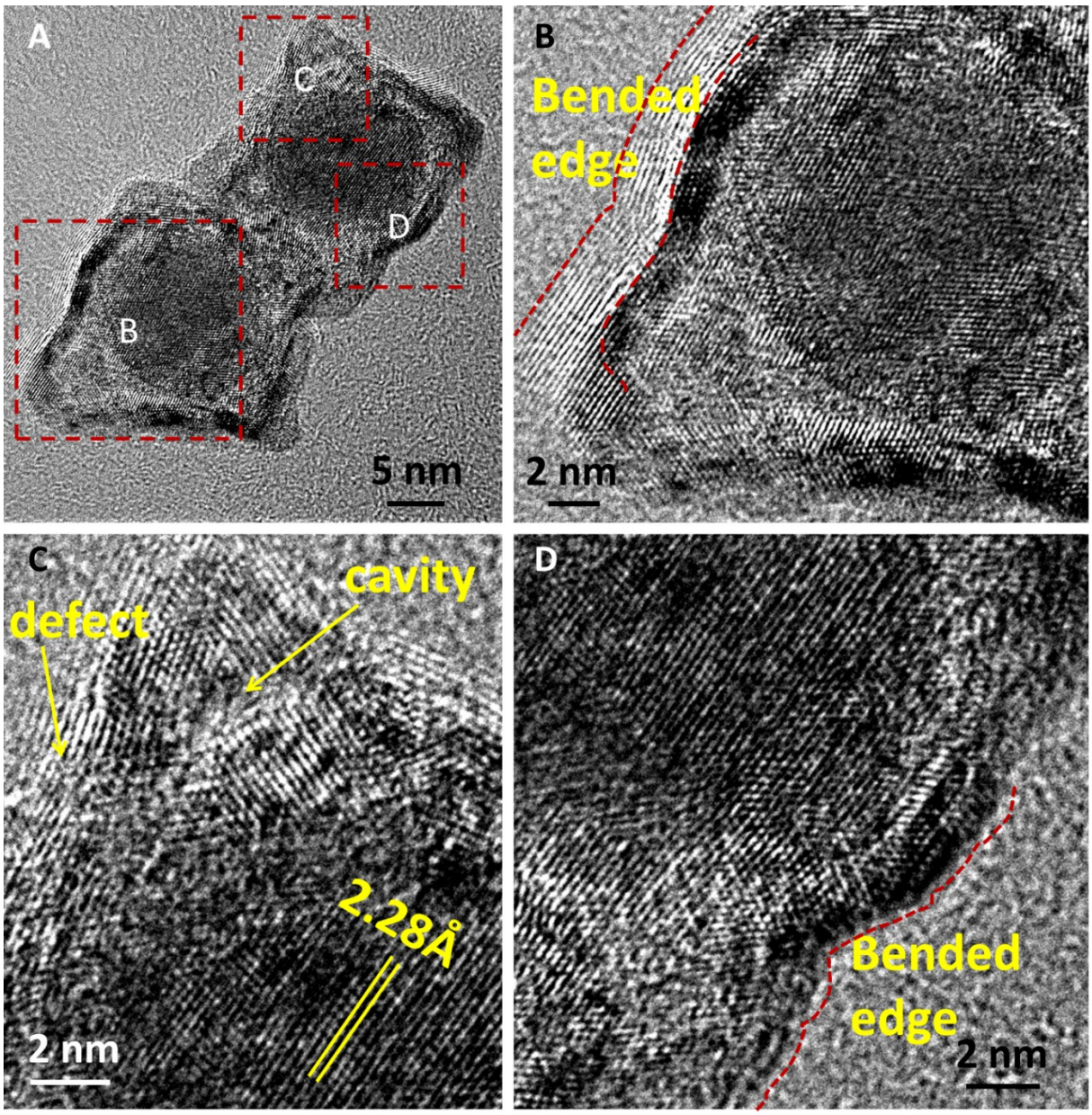

Fig. S6 (A) HRTEM image of Pt-Ni-Ir yolk-shell particles, and (B-D) three enlarged region circled by red rectangles. The distinct lattice fringes with a *d*-spacing of 2.28 Å coherently extended over the whole shell. Cavity and lattice defect were observed on the shell. The bended edges were also observed.

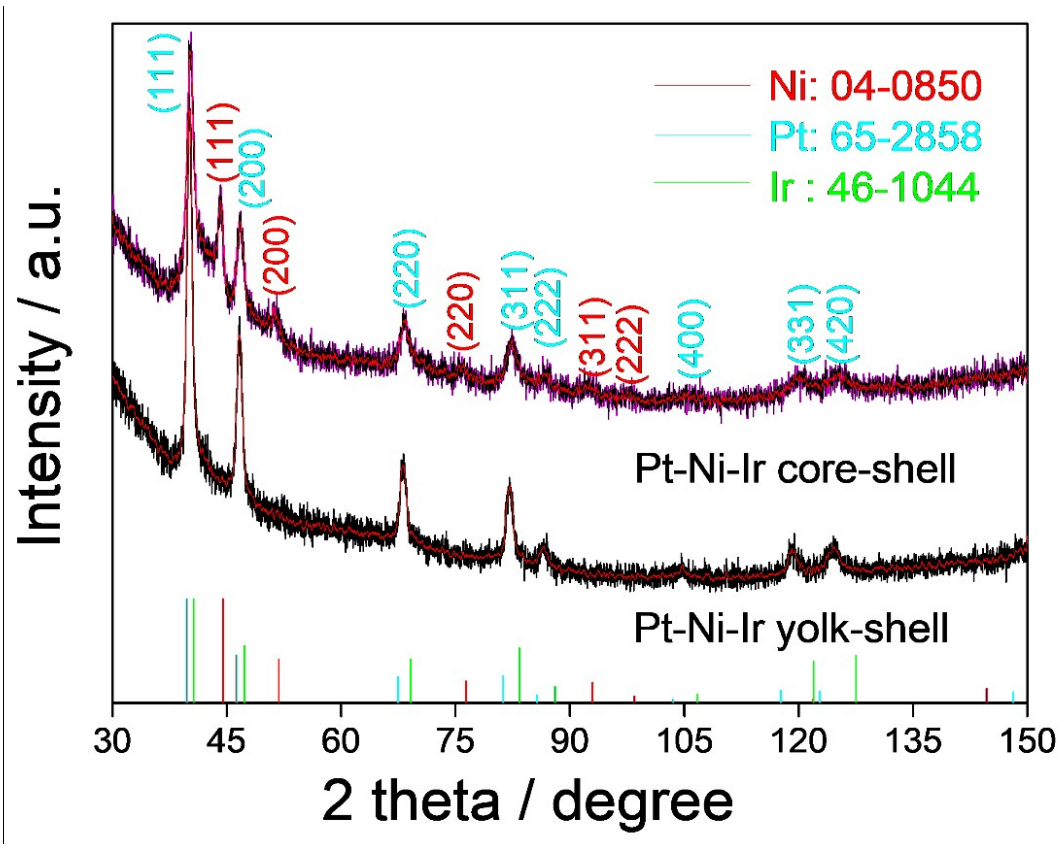

Fig. S7 XRD patterns of Pt-Ni-Ir core-shell and yolk-shell particles. The standard Pt, Ni and Ir peaks are marked as cyan, red and green lines perpendicular to the x-axis.

Table S1 XRD peaks analysis of Pt-Ni-Ir core-shell and yolk-shell nanostructures.

	(111)	(200)	(220)	(311)	(222)	(400)	(331)	(420)	(422)
Pt-Ni-Ir core-shell	40.223 44.267	46.762 51.541	68.348 76.042	82.425 91.94	86.546 96.98	104.94	119.58	124.84	
Pt-Ni-Ir yolk-shell	40.144	46.683	68.190	82.113	86.441	104.66	119.16	124.30	
Pt (#65-2858)	39.754	46.233	67.452	81.242	85.688	103.478	117.663	122.775	148.169
Ni (#04-0850)	44.507	51.846	76.370	92.944	98.446	121.930	144.669	155.653	
Ir (#46-1044)	40.660	47.303	69.134	83.412	88.035	106.714	121.942	127.556	

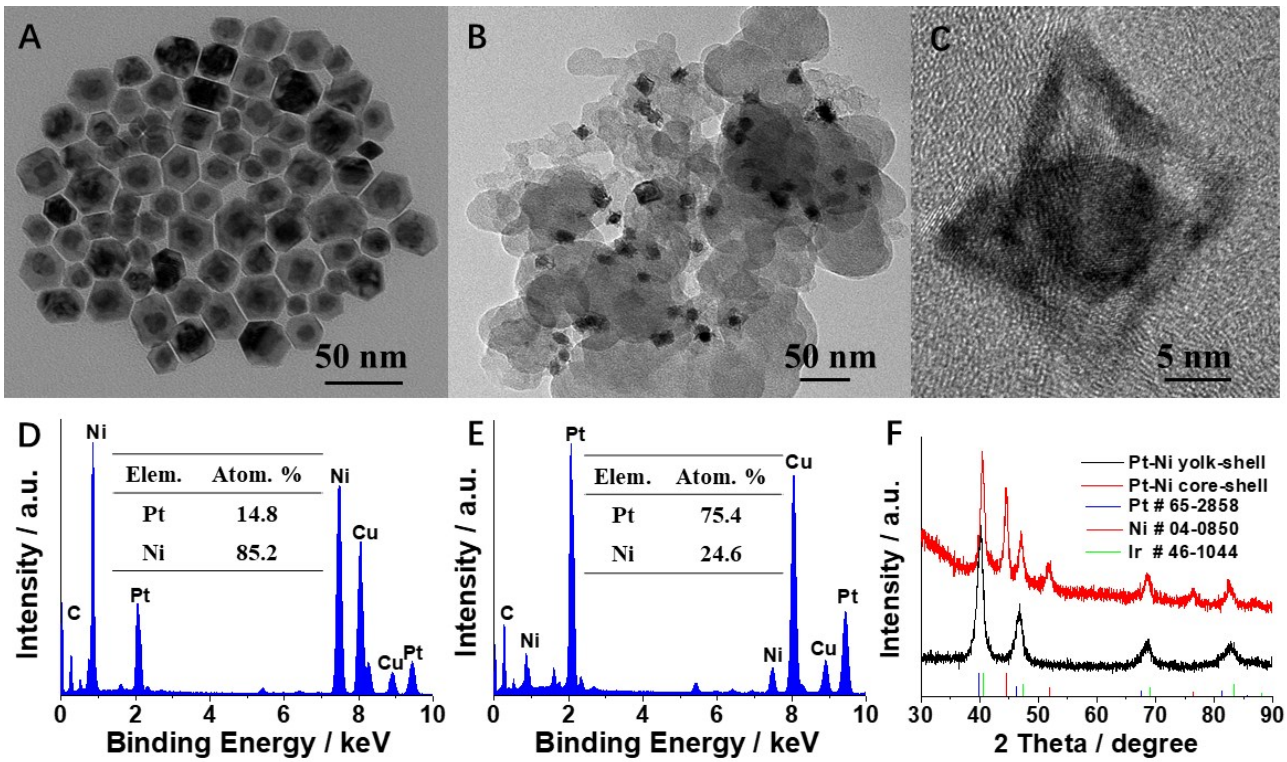

Fig. S8 Pt-Ni core-shell and yolk-shell nanostructures. TEM image of Pt-Ni (A) core-shell and (B) yolk-shell nanoparticles, (C) HRTEM image of Pt-Ni yolk-shell nanoparticle. TEM-EDS spectra and chemical composition of (D) core-shell and (E) yolk-shell nanostructures. (F) XRD pattern of Pt-Ni core-shell and yolk-shell nanoparticles. The Pt-Ni core-shell and yolk-shell were prepared through the same method of Pt-Ni-Ir core-shell and yolk-shell in absence of $Ir(acac)_3$.

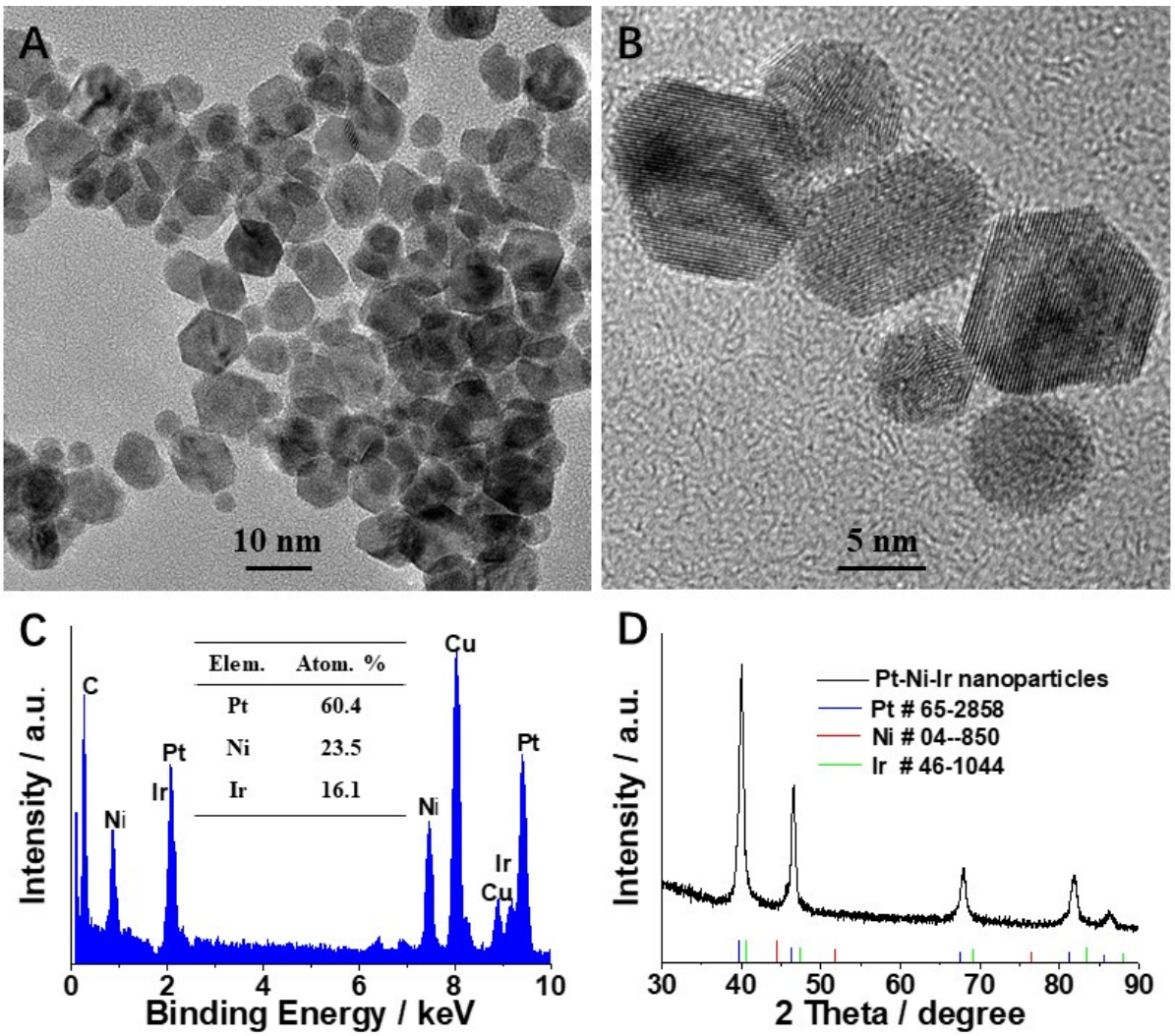

Fig. S9 Pt-Ni-Ir nanoparticles. (A) TEM image and (B) HRTEM image of the ternary alloy particles. (C) EDS spectra and chemical composition, (D) XRD of the ternary particles. Pt-Ni-Ir nanoparticles were prepared by reducing $Pt(acac)_2$ (20 mg, 0.051 mmol), $Ni(acac)_2$ (5 mg, 0.019mmol) and $Ir(acac)_3$ (10 mg, 0.02 mmol) in oleylamine (9.0 mL) and oleic acid (1.0 mL) with carbon monoxide at 230 ℃ for 60 min.

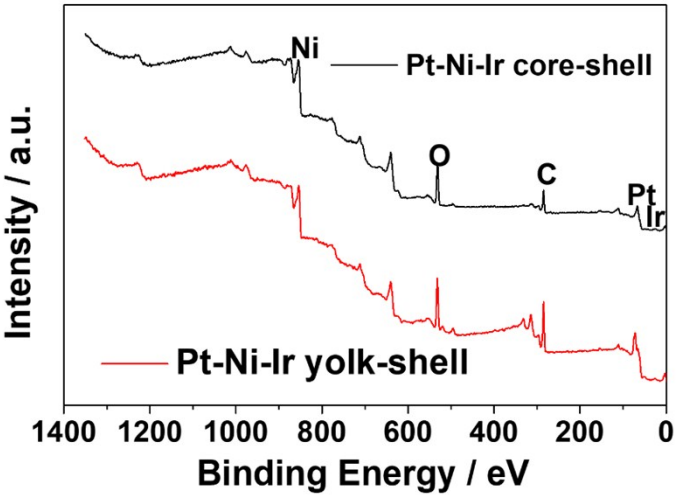

Elem.	Atom. %	
	Core-shell	Yolk-shell
Pt	0.96	60.69
Ni	96.15	14.33
Ir	2.89	24.98

Fig. S10 Overview XPS spectra of Pt-Ni-Ir core-shell and yolk-shell nanoparticles, and the corresponding chemical compositions.

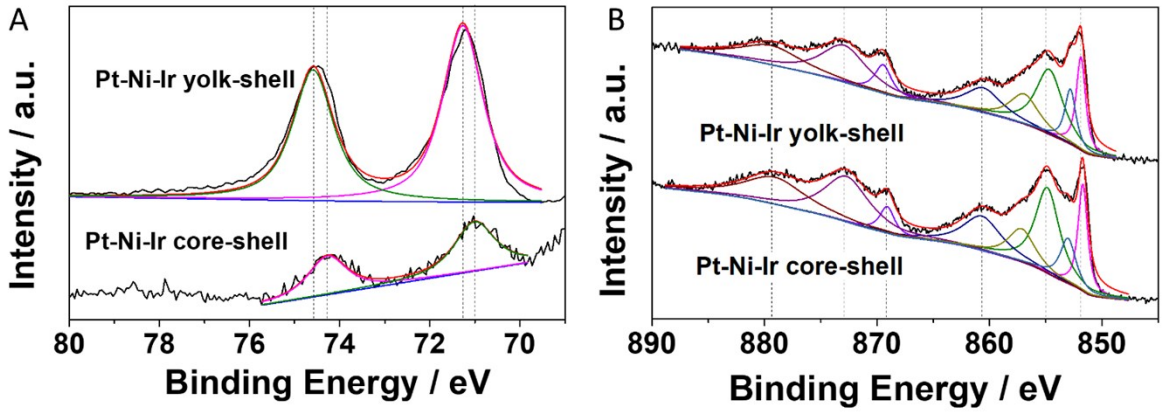

Fig. S11 High solution XPS spectra of (A) Pt and (B) Ni for Pt-Ni-Ir core-shell and yolk-shell particles. The Pt binding energy showed positive shift for Pt-Ni-Ir yolk-shell, suggesting a modification of electronic structure and binding properties.

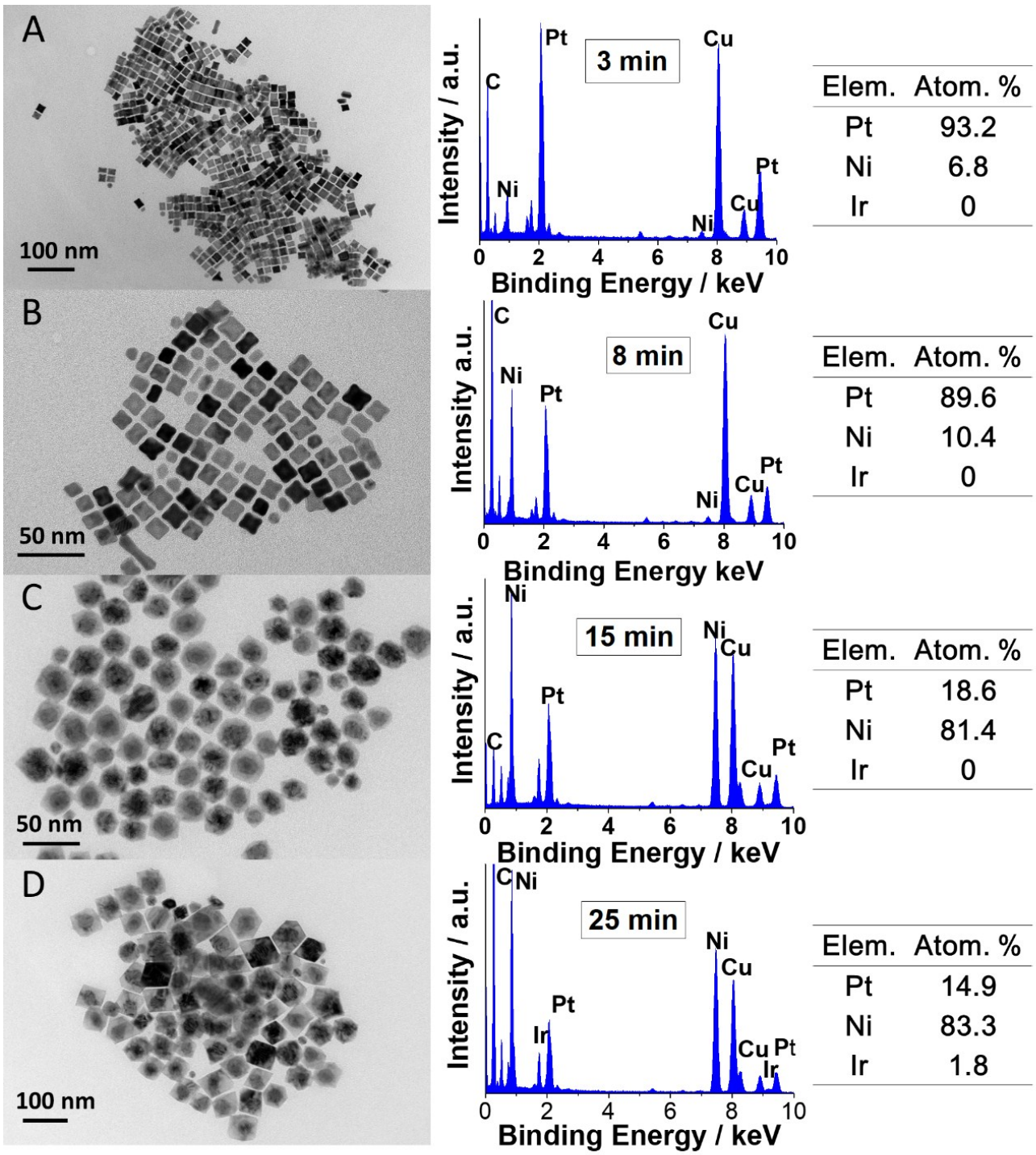

Fig. S12 TEM images of products obtained from first step of stepwise co-deposition process and the corresponding EDS spectra at different reaction time. (A) 3 min, (B) 8 min, (C) 15 min, (D) 25 min. The chemical compositions calculated from EDS spectra were also shown. The results show that cubic Pt-rich nanocrystals firstly formed at the initial stage, Ni-rich shell then deposited onto the nanocubes exclusively.

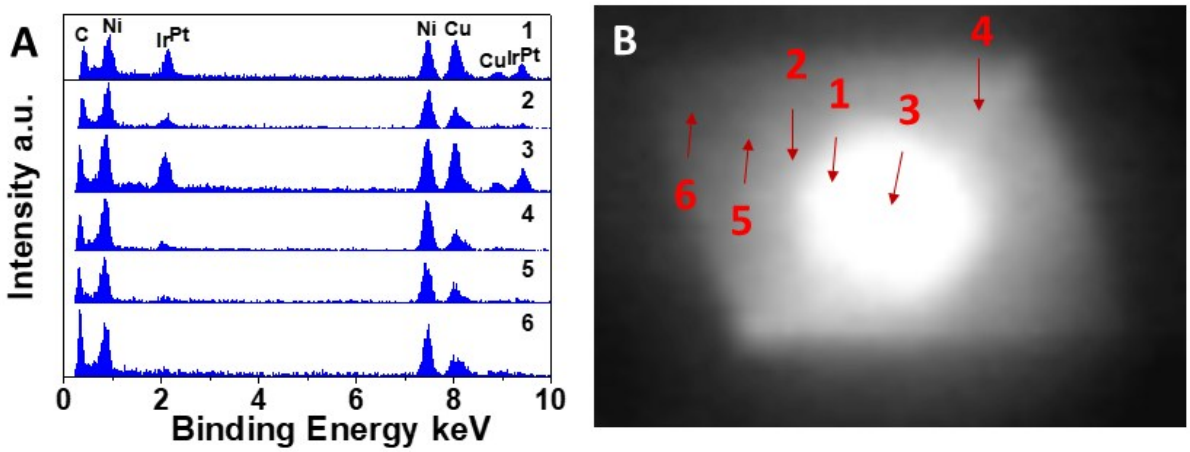

Fig. S13 EDS spectra from different location of the Pt-Ni-Ir core-shell nanoparticle.

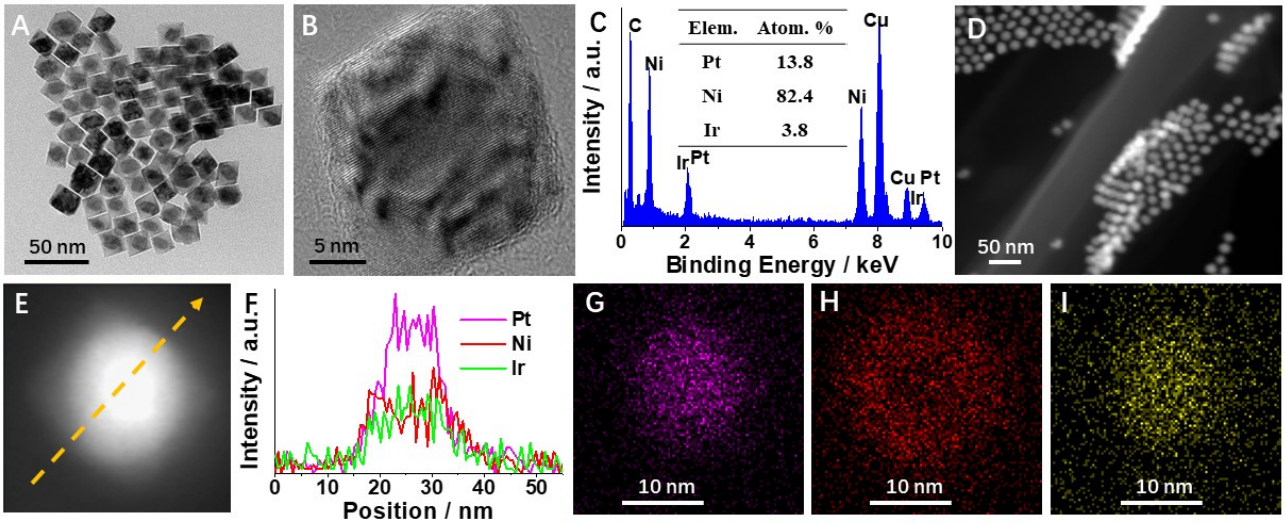

Fig. S14 (A) TEM image, (B) HRTEM image, (C) TEM-EDS, (D) STEM image, (E) Cross-sectional compositional line profile, elemental mapping for (G) Pt, (H) Ni and (Ir) on the Pt-Ni-Ir core-shell nanoparticle of (E). The product was obtained at 30 min in stepwise co-deposition process.

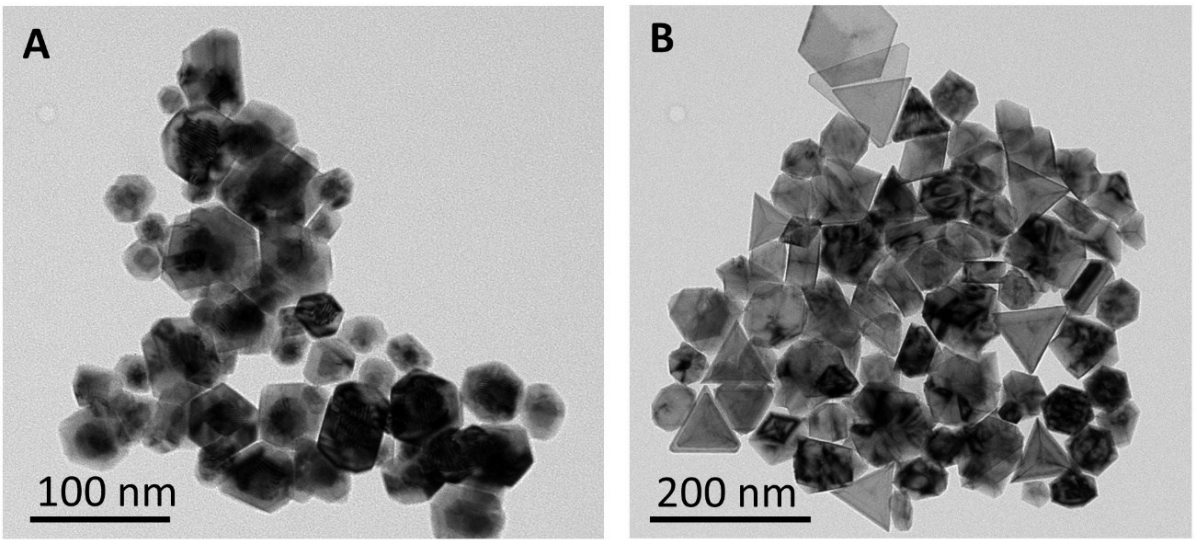

Fig. S15 Product without (A) $Ir(acac)_3$ or (B) $Pt(acac)_2$ in the stepwise co-deposition process.

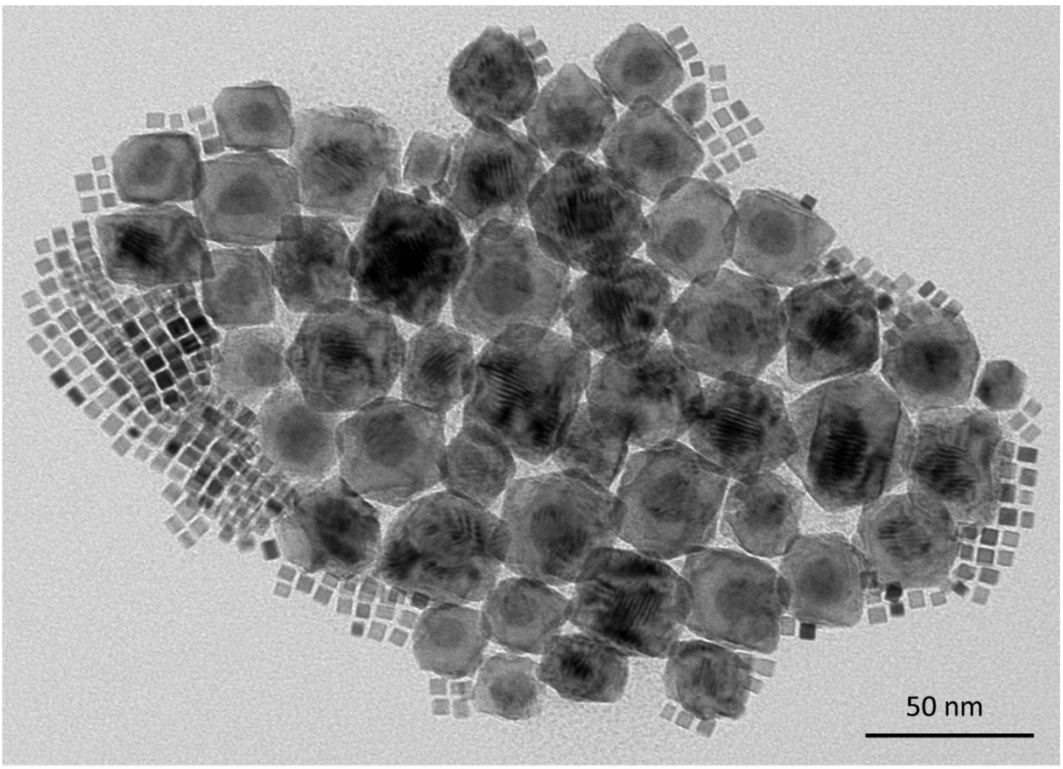

Fig. S16 TEM image of the product in the second step of controllable Pt deposition without using TOP. Cubic Pt nanocrystals also formed.

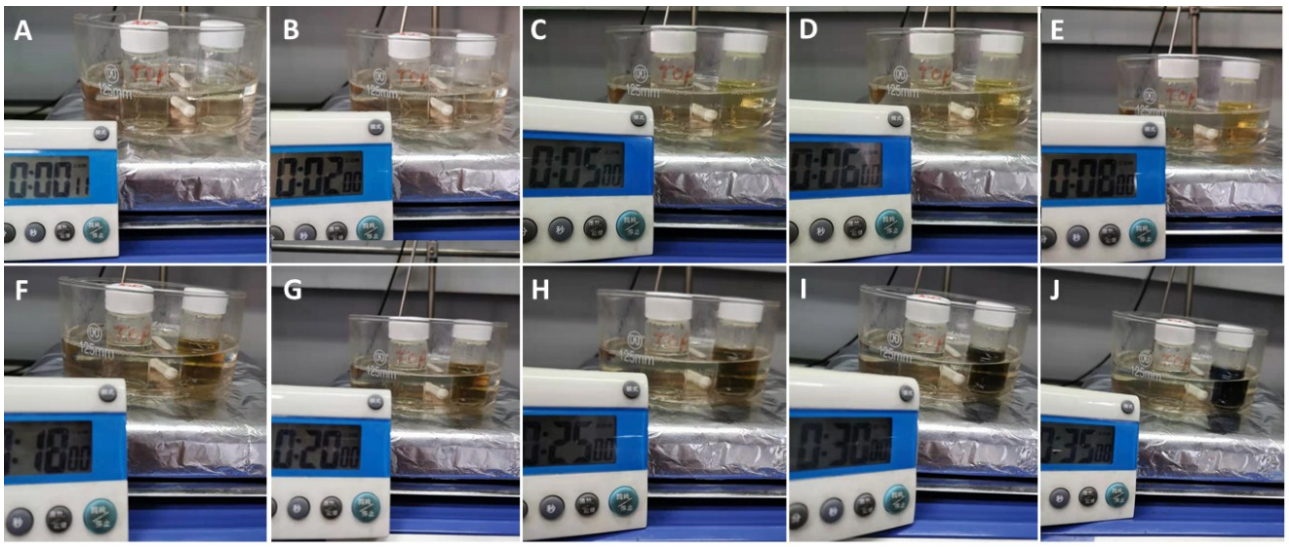

Fig. S17 The Influence of TOP on Pt deposition. A solution of oleylamine with $Pt(acac)_2$ and TOP remained colorless and transparent in 35 min at 180 ℃, suggesting that Pt has not been reduced. While a solution of oleylamine with only $Pt(acac)_2$ became more and more black, suggesting the Pt deposition.

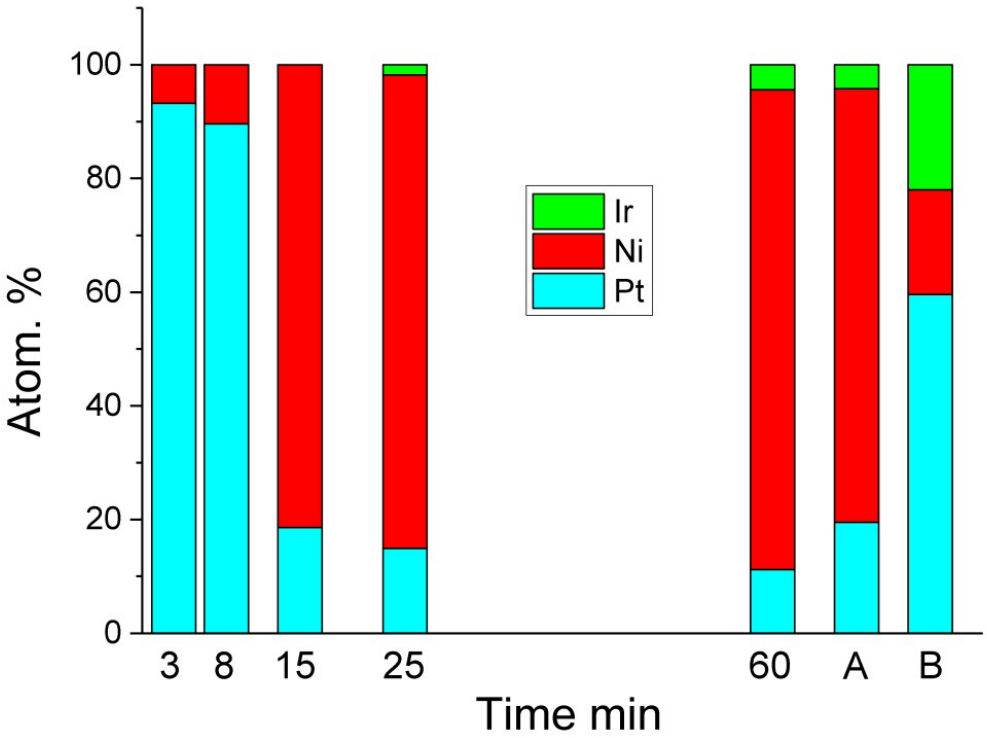

Fig. S18 Chemical composition evolution in the products at different reaction time. A is Pt covered Pt-Ni-Ir core-shell, B is Pt-Ni-Ir yolk-shell.

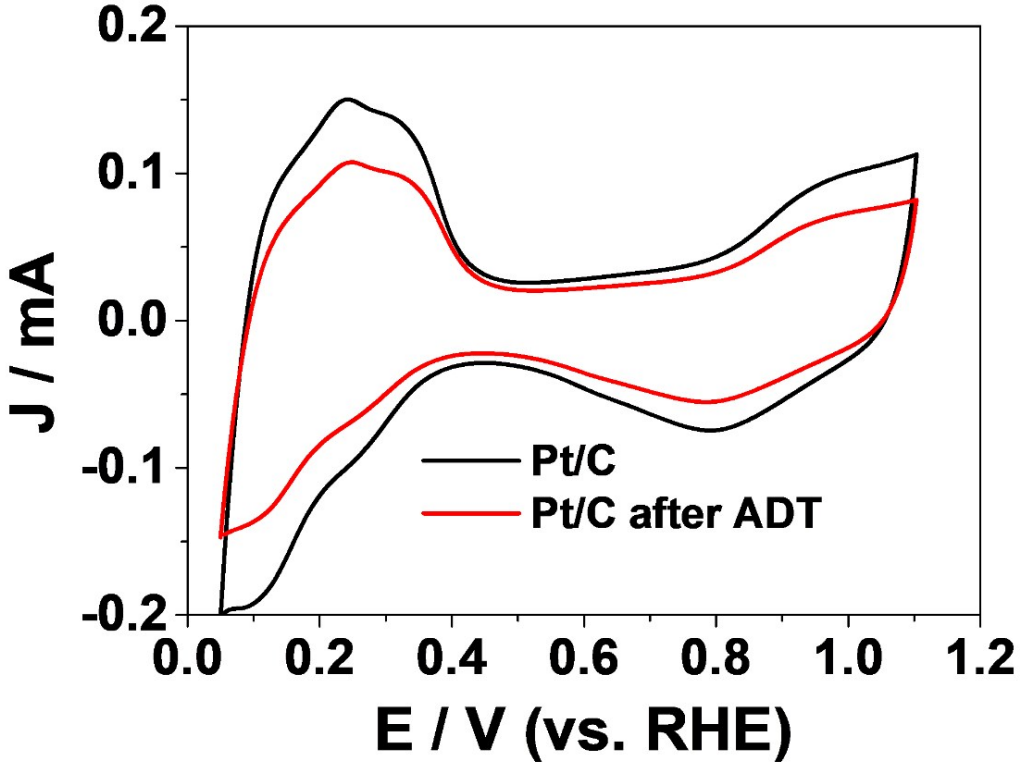

Fig. S19 CV profiles of commercial Pt/C before and after durability test for ORR in $HClO_4$ solution. The durability tests were performed by 10000 CV cycles in oxygen saturated $HClO_4$ solution in the potential range of 0.6-1.0 V.

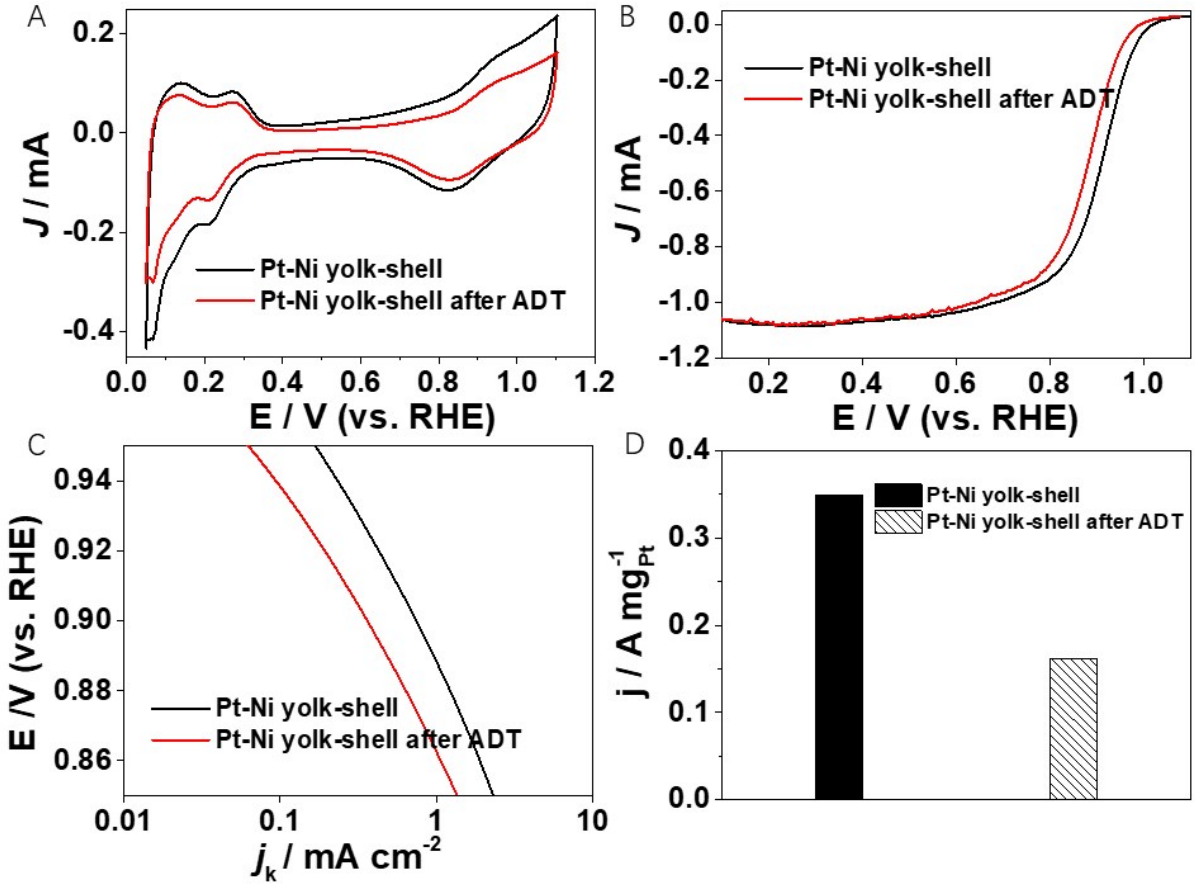

Fig. S20 ORR performance of Pt-Ni yolk-shell catalyst in $HClO_4$ before and after ADT test. (A) CV curves, (B) ORR polarization curves, (C) specific activities toward ORR (j_k) that are presented as kinetic current normalized to the EASA. (D) mass activities toward ORR based on Pt loading amount.

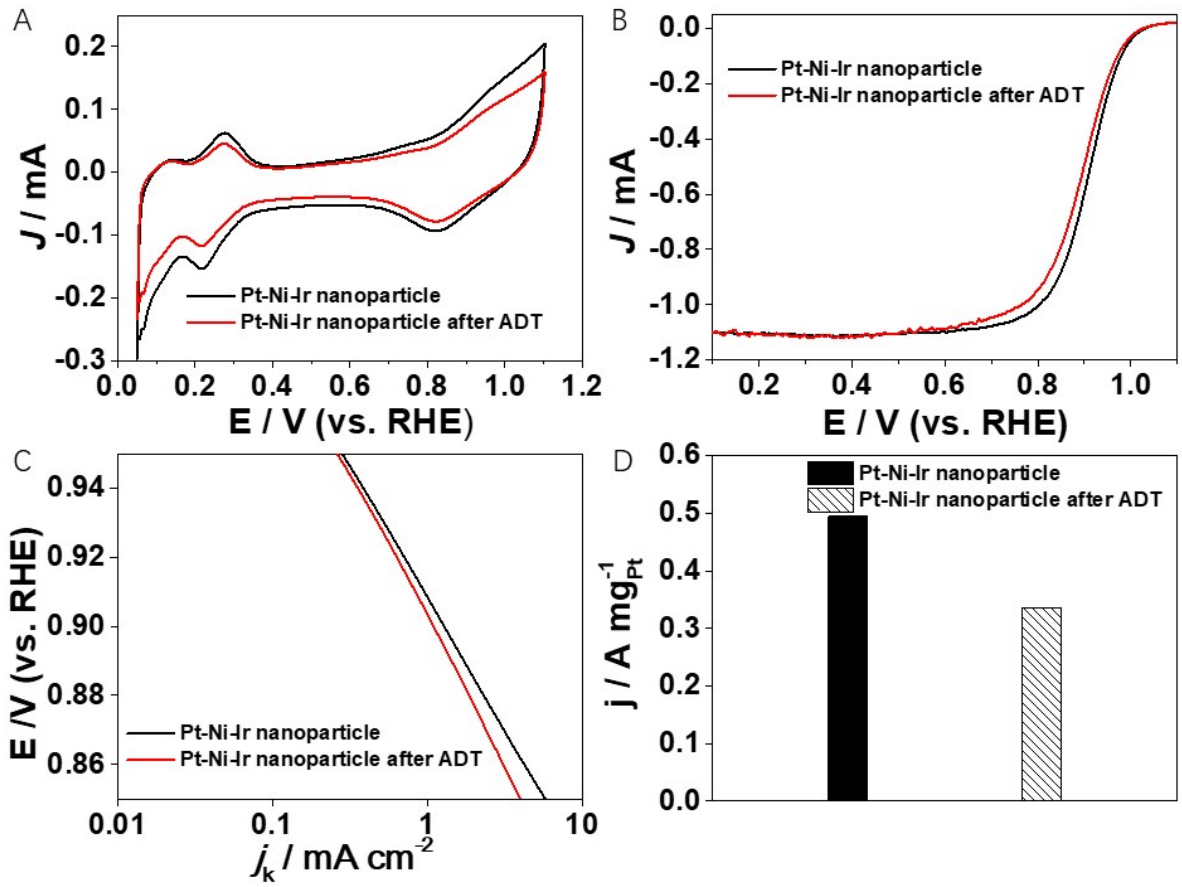

Fig. S21 ORR performance of Pt-Ni-Ir nanoparticle catalyst in $HClO_4$ before and after ADT test. (A) CV curves, (B) ORR polarization curves, (C) specific activities toward ORR (j_k) that are presented as kinetic current normalized to the EASA. (D) mass activities toward ORR based on Pt loading amount.

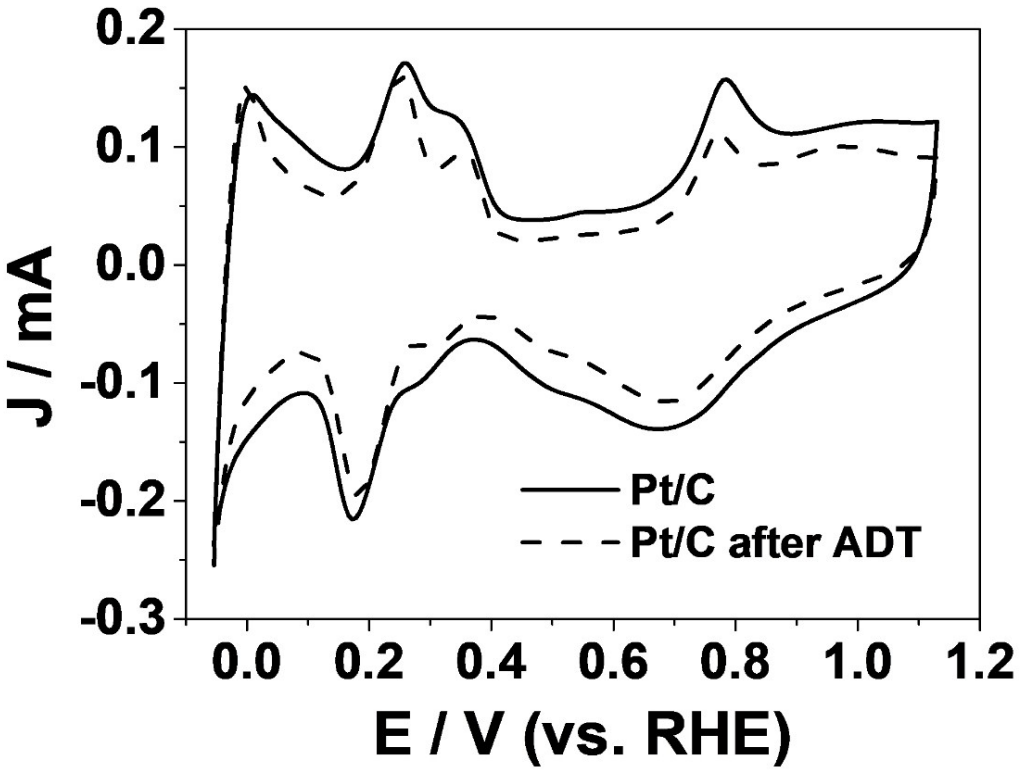

Fig. S22 CV profiles of commercial Pt/C before and after durability test for ORR in KOH solution. The durability tests were performed by 10000 CV cycles in oxygen saturated KOH solution in the potential range of 0.6-1.0 V.

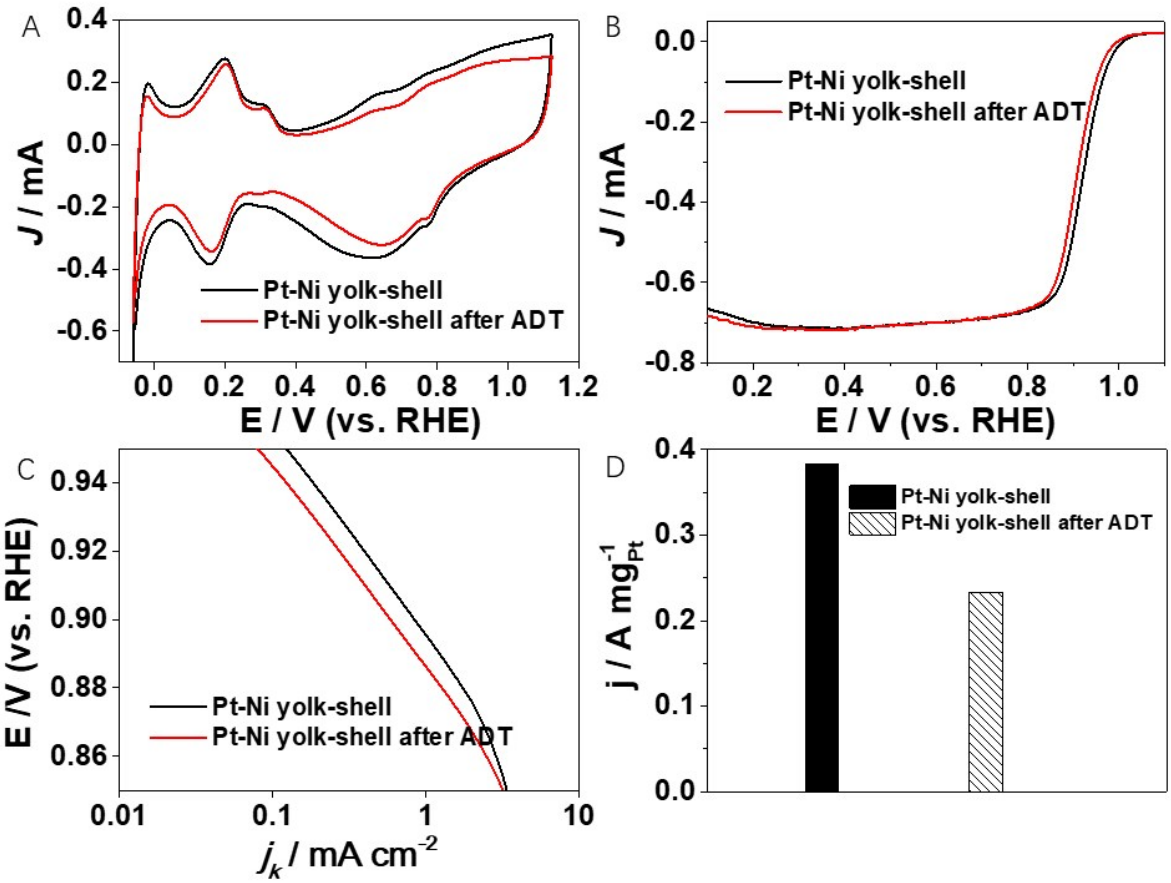

Fig. S23 ORR performance of Pt-Ni yolk-shell catalyst in KOH before and after ADT test. (A) CV curves, (B) ORR polarization curves, (C) specific activities toward ORR (j_k) that are presented as kinetic current normalized to the EASA. (D) mass activities toward ORR based on Pt loading amount.

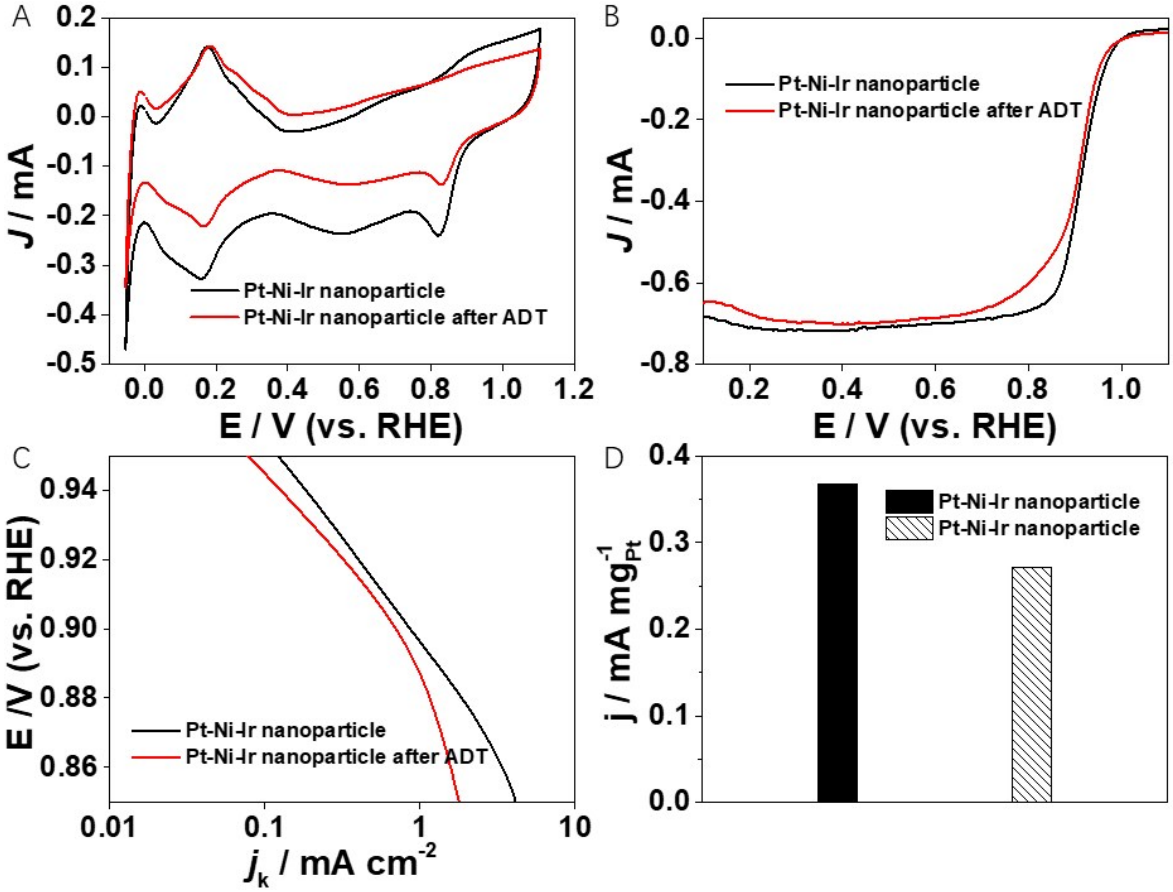

Fig. S24 ORR performance of Pt-Ni-Ir nanoparticle catalyst in KOH before and after ADT test. (A) CV curves, (B) ORR polarization curves, (C) specific activities toward ORR (j_k) that are presented as kinetic current normalized to the EASA. (D) mass activities toward ORR based on Pt loading amount.

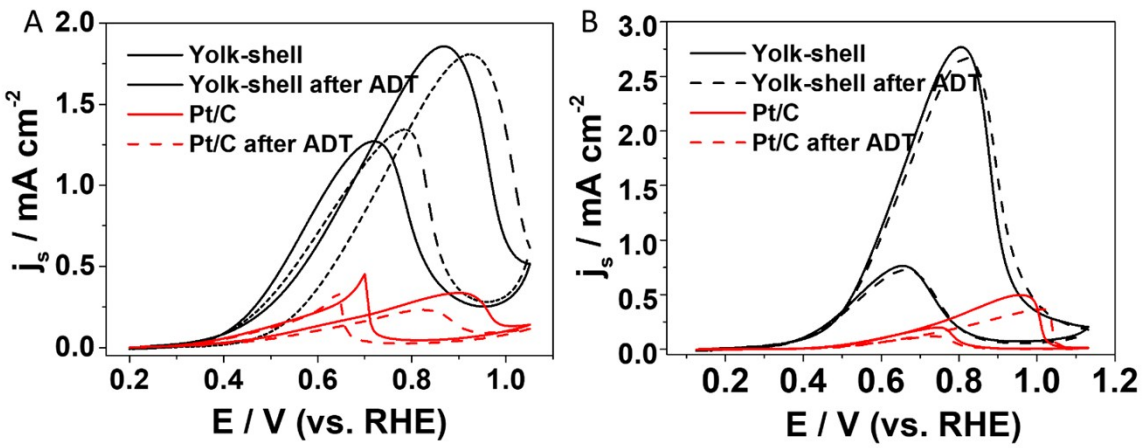

Fig. S25 Comparison of MOR electrocatalytic properties between Pt-Ni-Ir Yolk-shell and the commercial Pt/C catalysts. CV profiles in Ar-saturated (A) 0.1 M $HClO_4$ + 1 M CH_3OH and (B) 1.0 M KOH +1 M CH_3OH solution, respectively. The current was normalized to ECSA of the catalysts. The durability tests were performed by 4000 MOR CV cycles in the solution of 0.1 M $HClO_4$ + 1 M CH_3OH and 1.0 M KOH +1 M CH_3OH solution, respectively.

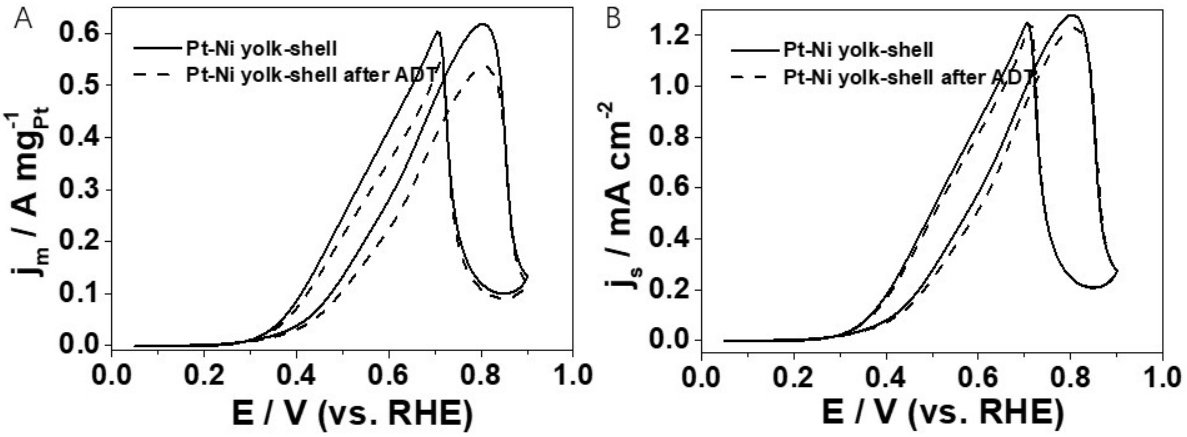

Fig. S26 MOR CV profiles of Pt-Ni yolk-shell catalyst before and after ADT test in 0.1 M $HClO_4$ + 1 M CH_3OH. (A) Mass activities, the current was normalized to Pt loading amount, (B) specific activity, the current was normalized to ECSAs.

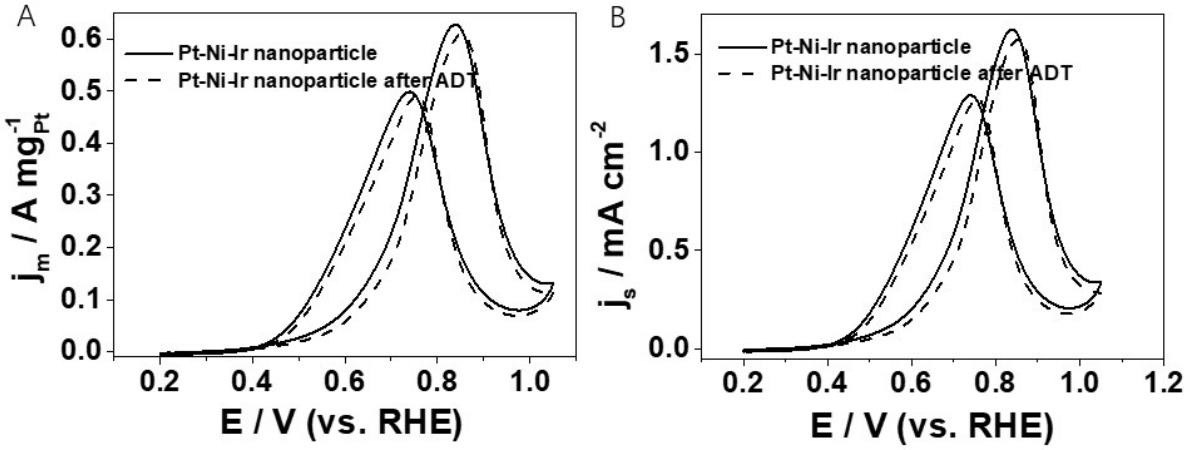

Fig. S27 MOR CV profiles of Pt-Ni-Ir nanoparticle catalyst before and after ADT test in 0.1 M $HClO_4$ + 1 M CH_3OH. (A) Mass activities, the current was normalized to Pt loading amount, (B) specific activity, the current was normalized to ECSAs.

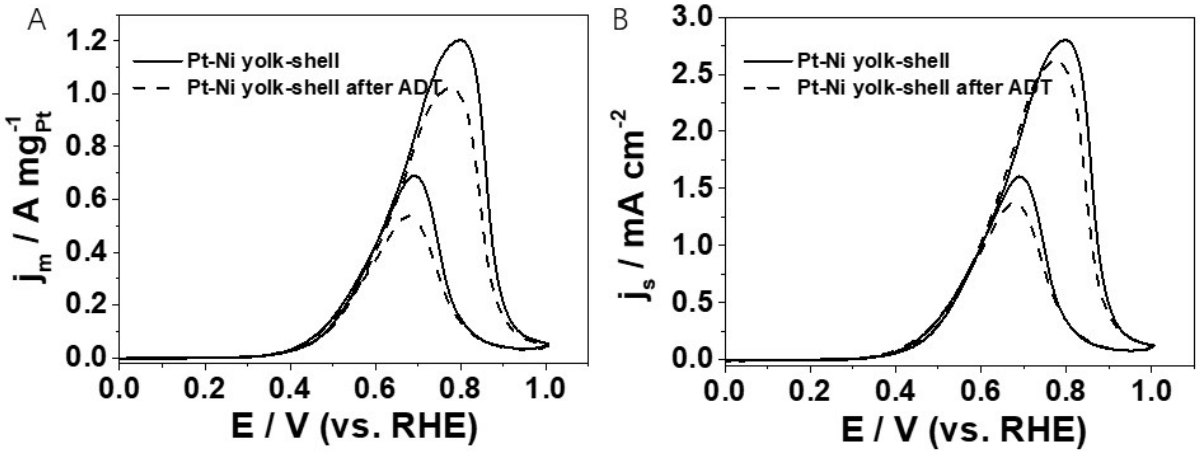

Fig. S28 MOR CV profiles of Pt-Ni yolk-shell catalyst before and after ADT test in 1.0 M KOH + 1.0 M CH_3OH. (A) Mass activities, the current was normalized to Pt loading amount, (B) specific activity, the current was normalized to ECSAs.

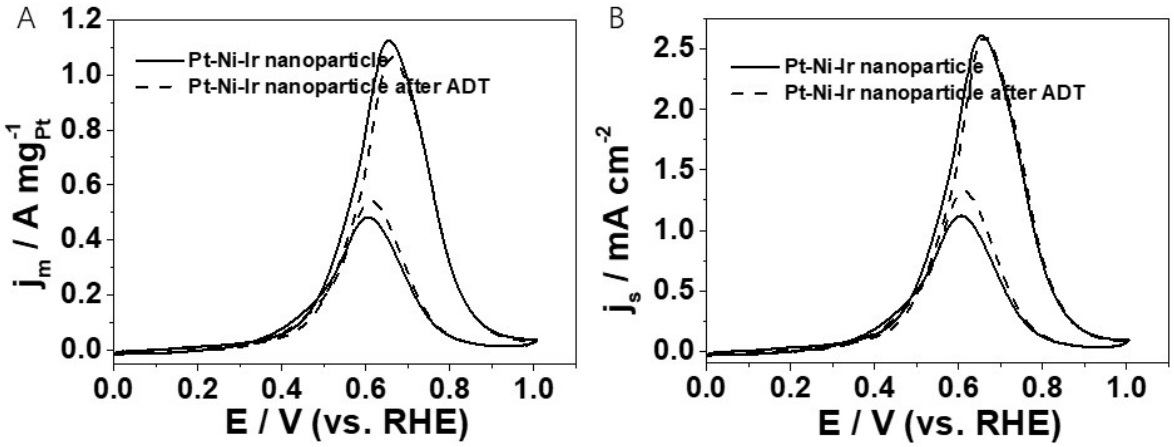

Fig. S29 MOR CV profiles of Pt-Ni-Ir nanoparticle catalyst before and after ADT test in 1.0 M KOH + 1.0 M CH_3OH. (A) Mass activities, the current was normalized to Pt loading amount, (B) specific activity, the current was normalized to ECSAs.

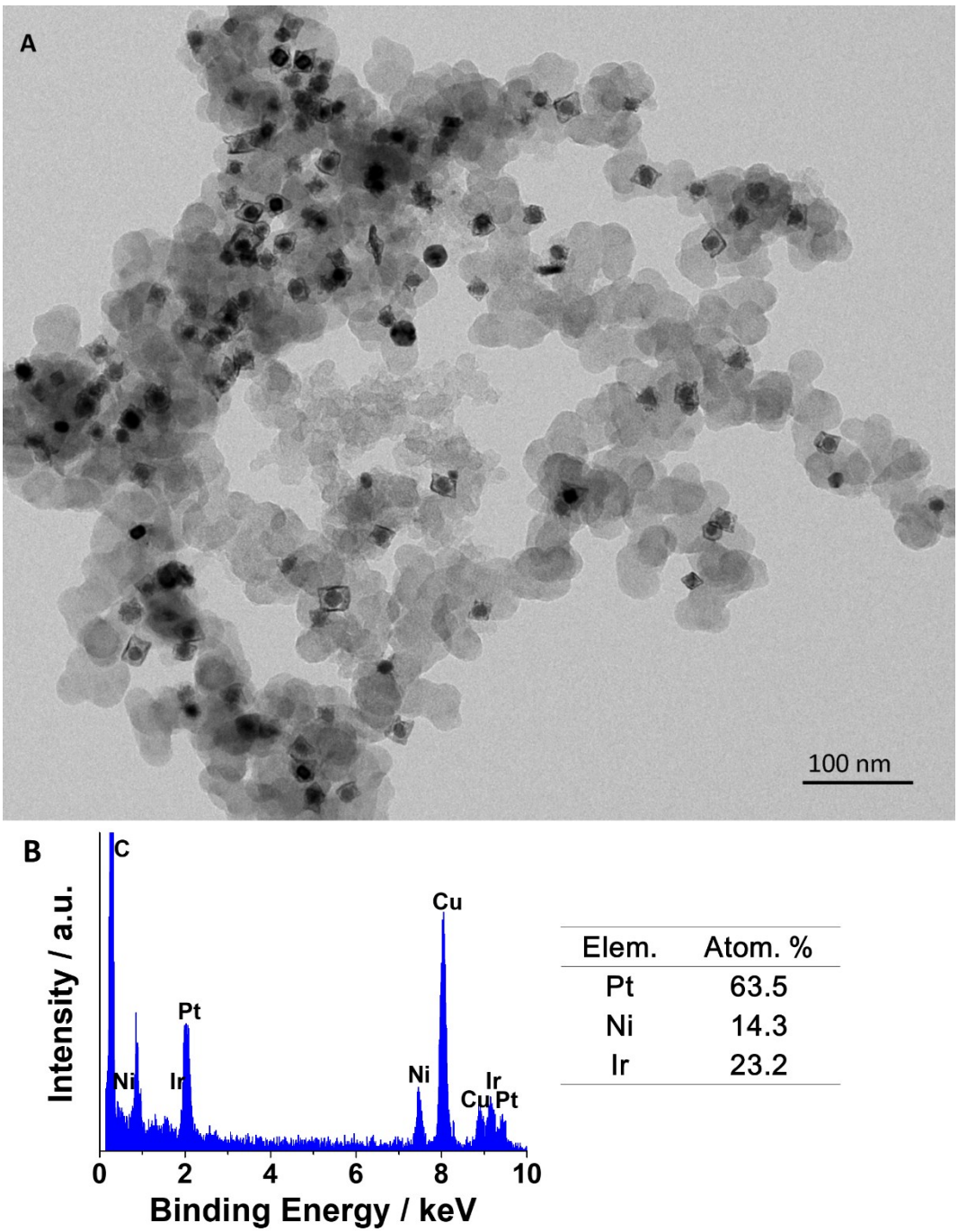

Elem.	Atom. %
Pt	63.5
Ni	14.3
Ir	23.2

Fig. S30 (A) TEM image of the yolk-shell Pt-Ni-Ir catalyst after ORR durability test in $HClO_4$ solution, and (B) the corresponding EDS spectra. The chemical composition calculated from EDS spectra was shown. Compared with the initial yolk-shell catalyst, the Ni content decreased from 18.4 % to 14.3 %.

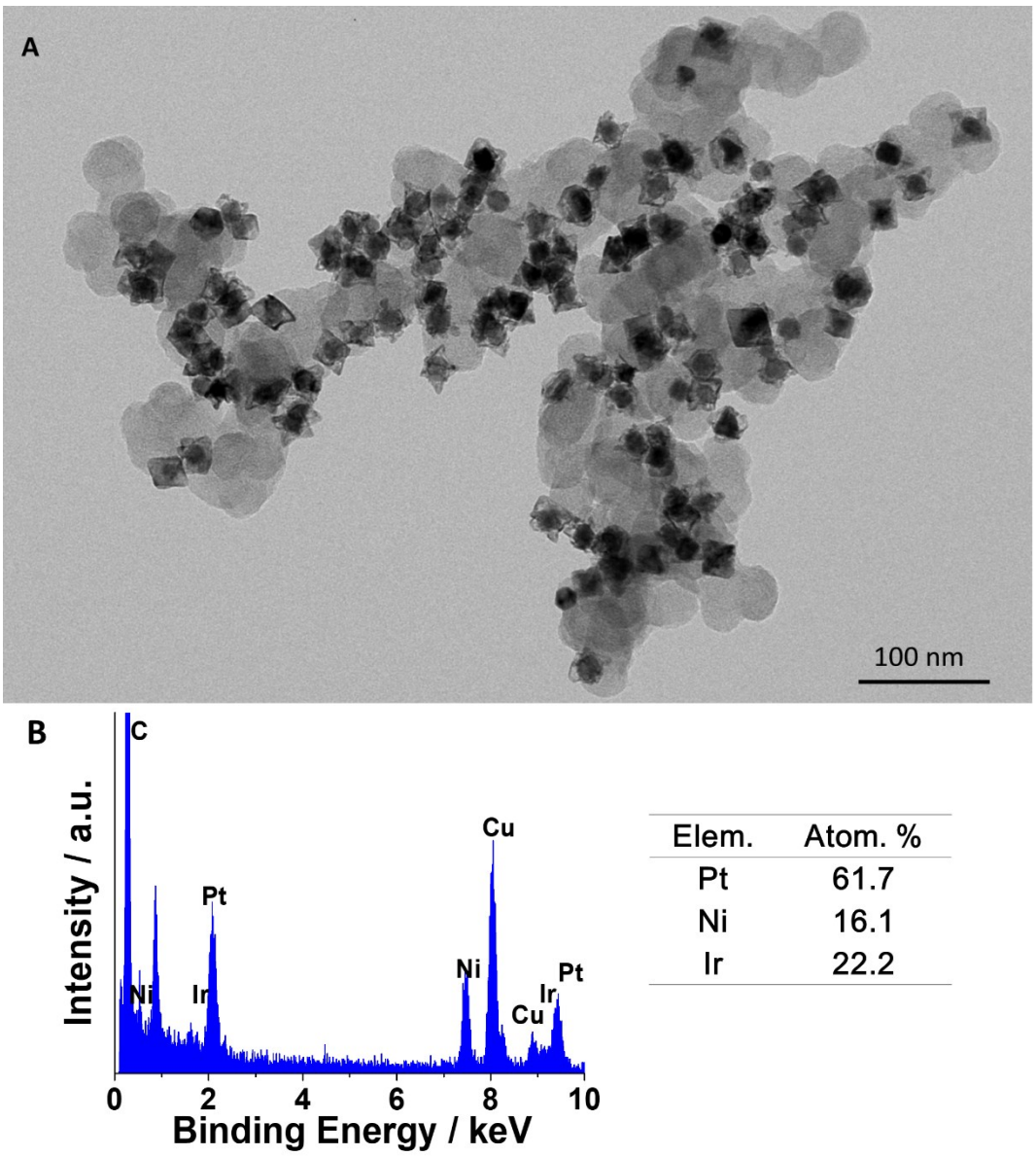

Elem.	Atom. %
Pt	61.7
Ni	16.1
Ir	22.2

Fig. S31 (A) TEM image of the yolk-shell Pt-Ni-Ir catalyst after MOR durability test in $HClO_4$ +CH_3OH solution, and (B) the corresponding EDS spectra. The chemical composition calculated from EDS spectra was shown. Compared with the initial yolk-shell catalyst, the Ni content decreased from 18.4 % to 16.1 %.

Table S2 The ECSA and specific activities variation through the ORR durability test in $HClO_4$ solution.

Samples	EASA m^2g^{-1}		Degraded %	J_k @ 0.9 V mA cm^{-2}		Degraded %
	Initial	Final		Initial	Final	
Commercial Pt/C	64.3	48.1	25.2	0.22	0.106	51.8
Pt-Ni yolk-shell	48.3	35.6	26.2	0.72	0.45	53.6
Pt-Ni-Ir nanoparticle	38.7	30.0	22.6	1.28	1.12	31.9
Pt-Ni-Ir Yolk-shell	42.1	33.3	21	1.58	1.54	2.5

Table S3 The ECSA and specific activities variation through the ORR durability test in KOH solution.

Samples	EASA m^2g^{-1}		Degraded %	J_k @ 0.9 V mA cm^{-2}		Degraded %
	Initial	Final		Initial	Final	
Commercial Pt/C	66.1	59.9	9.4	0.205	0.137	33.2
Pt-Ni yolk-shell	45.7	39.8	13	0.84	0.59	31
Pt-Ni-Ir nanoparticle	42.8	39.0	8.9	0.86	0.70	26.2
Pt-Ni-Ir Yolk-shell	40.7	43.4	-6.6	0.961	0.707	26.4

Table S4 The MOR peak mass activities through the durability test.

Samples	$HClO_4$ mA mg_{Pt}^{-1}		Degraded %	KOH mA mg_{Pt}^{-1}		Degraded %
	Initial	Final		Initial	Final	
Commercial Pt/C	216	149	31	319	236	26
Pt-Ni yolk-shell	618	536	13.3	1203	1019	15.3
Pt-Ni-Ir nanoparticle	628	611	2.7	1124	1068	5
Pt-Ni-Ir Yolk-shell	782	760	2.7	1165	1123	3.6